



VIRTUAL REALITY SCENARIO ANALYSIS OF ART DESIGN TAKING INTO ACCOUNT INTERACTIVE DIGITAL MEDIA PATTERN GENERATION TECHNOLOGY

YUN LIU *

Abstract. In art design, 3D printing technology is crucial, and more and more creators conceive scenes using 3D modeling software to get a three-dimensional and beautiful work. Due to the large amount of noise and redundant points in the raw data collected during the modeling process, the generation speed and rendering effect of 3D models are reduced. Given the above problems, the study designed an interactive 3D lightweight modeling system based on the combination of hand-drawn sketching and laser 3D scanning based on the streamlined algorithm. The experimental results showed that when the hand-drawn speed was 300, the number of triangular slices, model size, and time required to generate the model of the hand-drawn sketching model based on the streamlined algorithm were reduced by 67.39%, 65.48%, and 63.79%, respectively. In the real-time point cloud data streamlining process of the laser 3D scanning model, the point cloud data reduction ratio and the streamlining goodness index of the point cloud streamlining algorithm are 71.99% and 3.06%, respectively. The system performance is robust, and the data processing speed and rendering effect are good.

Key words: : hand sketching, laser scanning, Three-dimensional modeling, real-time resampling, latitude and longitude line refinement method

1. Introduction. Virtual and real is an important aesthetic principle in art creation, and its application to artworks can effectively highlight the uniqueness of the works [4]. With the popularization of 3D printing technology, the art design based on virtual reality is no longer satisfied with the traditional drawing on paper, but gradually developed into three-dimensional modeling works [19, 18]. 3D modeling works with complete details, and more comprehensive treatment of reality and darkness can better help the public to understand the three-dimensional artworks and facilitate the appreciation of the works from multiple perspectives [16]. Traditional 3D modeling has a high threshold, its data is less streamlined, and the resulting 3D model is less well rendered, which cannot meet the public's and designers' needs. Hand-drawn sketch (HS) 3D modeling based on digital boards is interactive and real-time, but there are more noise and redundant points in the collected data, affecting the model's rendering effect [15]. Laser Scanning (LS) is to obtain 3D point cloud data by measuring the physical surface; this modeling method has high measurement speed and accuracy, but too much data collection is not conducive to network data transmission [13, 17]. To address the problem of high data density, noise, and redundancy, the study proposes an interactive three-dimensional lightweight (ITL) modeling system that combines HS and LS based on traditional 3D modeling. The first point is that the research uses a real-time streamlining algorithm to streamline the noise and redundant points in the collected data, to ensure the rendering effect of the model; the second point is that the HS and LS modeling methods are integrated into the traditional 3D modeling, and the online ITL modeling system is obtained. The structure of the research is divided into four main parts, the first part is a review of related research results; the second part is based on the design of HS and LS models and the integration of HS and LS into traditional 3D modeling to obtain the ITL modeling system; the third part is the validation of the effectiveness of the modeling system proposed by the research; the last part is the summary of the research results. Table 1.1 lists technical terms involved in the study.

2. Related works. Traditionally, 3D modeling is mostly based on the function menu and icons of software pages, using a keyboard and mouse to create regular geometry models. However, this kind of human-computer interaction based on a keyboard and mouse is poor and cannot meet the popular demand. To improve the

*Hunan Mass Media Vocational and Technical College, Changsha, 410100, Hunan, China (liuyun202302@126.com)

Table 1.1: Technical Terminology Involved in the Research

Technical terminology	Meaning
HS	Hand-drawn sketch
LS	Laser Scanning
ITL	interactive three-dimensional light-weight
SWR	Sliding Window Reduction
CR	the streamlining ratio
E_{max}	The local maximum distance error
E_i	The overall length error
SCS	Single-stroke Closed Sketch
SUS	Single-stroke Unclosed Sketch
LALS	Latitude And Longitude Simplification
R_r	The reduction ratio
E_{dis}	The streamlining error
FOM_a	The streamlining goodness index
T_s	The point cloud streamlining processing time
R_F	The model size reduction ratio
E_{TBL}	The light-weighting error
FOM_b	The goodness of light-weighting index
T_R	The generated model time

retrieval speed and human-computer interaction of 3D models, Shi X et al. designed an HS-based 3D retrieval algorithm, which simulates the ganglion perception mechanism in the retina and uses support vector machines to optimize the retrieval results. The experimental results show that the HS-based 3D retrieval algorithm can improve the retrieval accuracy [12]. Bai J et al. propose an end-to-end HS 3D model retrieval method based on joint embedding of spatiotemporal information to improve the retrieval effect, and the simulation results confirm the feasibility and effectiveness of the retrieval method [2]. Ito T et al. propose an end-to-end HS 3D model retrieval method based on joint embedding of spatio-temporal information to improve the retrieval effect. (CAD) The system's editing operation of drawing strokes can only target a single geometric object at a given time, and a general HS page-based 2D CAD system was proposed. It is shown that the HS-based CAD system is practical and convenient for beginners to operate and use [6]. Sarvadevabhatla R et al. proposed a deep neural model based on the incremental accumulation of HS stroke sequences as visual data, which can generate guesswords in response to HS and thus amplify the ability of intelligent machines to imitate humans. Experimental results demonstrate that the model can effectively respond to HS [11]. Donati L et al. designed a Pearson correlation-based line extraction algorithm and unbiased refinement algorithm for accurate and reliable vectorization of HS to construct 3D models, and simulation results confirm that the algorithm can efficiently and quickly complete HS vectorization [9].

Fancourt H et al. designed a fast 3D computerized shape analysis method to improve the classification efficiency of mixed skeletons and streamline the amount of 3D point cloud data for whole bone matching of 14 test samples [5]. Pistilli F et al. designed a deep learning algorithm using a graphical convolutional neural network to reduce noise and remove outlier points from point cloud data. The study was compared with other denoising methods. The algorithm can effectively deal with irregular regions and point cloud alignment invariance problems and construct complex domain graph feature hierarchies based on the similarity feature of points [10]. Zhang Z H designed a curvature and random filtering-based point cloud denoising algorithm to remove obvious noise points and random noise points in point cloud data and also used a bilateral filtering algorithm to perform point cloud smoothing after using this algorithm for denoising. The simulation results show that the error of the point cloud data processed by the denoising algorithm is smaller than that of the unprocessed point cloud data, confirming the algorithm's reliability [20]. Wu Q et al. proposed a linear LS-based method to measure the thickness of the thermal protection layer of solid rocket motors to

determine the thickness of the thermal protection layer of solid rocket motors. They used the octree-based streamlining algorithm to denoise and simplify the collected point cloud data. The results confirm that the linear LS and the octree-based streamlined algorithm are robust and can effectively measure the thickness of the thermal protection layer [14]. Chen H designed a point cloud denoising network combining recurrent network structure, convolutional neural network-based multi-scale feature aggregation module, circular propagation layer, and feature perception for denoising the 3D point clouds captured by depth cameras and 3D scanners. The experimental results demonstrate the superior performance of the denoising network and significantly improve the denoising efficiency of the point cloud data [3].

In summary, there are many research results on HS and LS modeling, but data processing based on HS modeling mainly focuses on segmentation and retrieval of HS and rarely involves real-time data streamlining; the data processing time of the point cloud denoising algorithm based on LS modeling is long, and the streamlining effect also needs to be improved. To address the problem of the modeling data streamlining effect being less than ideal, the study designs an ITL modeling system combining HS and LS based on traditional 3D modeling.

3. Methods. The acquisition of raw data is the prerequisite and foundation of 3D modeling, but in the acquisition process, there is more noise and a redundant amount of raw data memory. To improve the modeling real-time speed and rendering effect, the study introduces the streamlining algorithm to streamline the data in real time, and the chapter focuses on the design of the HS model and LS model based on the streamlining algorithm.

3.1. Establishment of HS model based on real-time data streamlining. As a common interactive model, the HS data essence is a series of discrete point series composed of auxiliary information such as serial number, time stamp, and speed. A large amount of noise and redundant points exist in the raw HS data, which can affect the data transmission within the system and thus degrade the quality of 3D modeling. To reduce the redundant data in HS, the study utilizes the chord length limit method to resample the data acquisition process in real-time [7]. The real-time resampling process of the chord length limit method is as follows, firstly, sketch and acquire the sketch trajectory start point P_1 , then move the digital pen to acquire the trajectory point P_2 and calculate the chord length l_{12} of $\overline{P_1P_2}$, to determine whether the chord length l_{12} is larger than the threshold value l_ε . If the chord length is larger than the threshold, keep P_2 as the starting point and calculate the chord length l_{23} , if the chord length is smaller than the threshold, delete the point and calculate the chord length l_{13} until the chord length is larger than the threshold. The threshold value of l_ε is given in equation (1).

$$l_\varepsilon = \chi \cdot \left(\frac{\sqrt{l_m^2 + w_m^2}}{d_m \cdot dpi} + n \right) \quad (3.1)$$

In equation 3.1, χ is the data streamlining factor, which takes the value of [0.6, 1.2]. l_m The horizontal resolution, vertical resolution, and diagonal length of the monitor are represented by w_m , h_m and d_m , respectively. n is the parameter that controls the ratio of ppi and dpi , where ppi and dpi are the monitor pixel density and standard pixel density, respectively, and $dpi = 160px/inch$ [8]. After real-time resampling, non-critical vertices in the original data can still be streamlined. To address this problem, the study invokes the length error E_l to replace the discrete point local curvature and designs a Sliding Window Reduction (SWR) algorithm to streamline the resampled data in real-time. The length error E_l is shown in equation (2).

$$E_l = (L_{sum} - L) / L_{sum} \times 100\% \quad (3.2)$$

In equation (3.2), L and L_{sum} represent the length of the line segment at the first and last endpoints within the sliding window and the sum of the lengths of the line segments between two adjacent points, respectively. The expression of the SWR algorithm is shown in Figure 3.1.

Figure 3.1(a) and Figure 3.1(b) show the sliding window-based length error limit algorithm and the vertical distance limit algorithm, respectively. The length error limit algorithm initially removes the obvious redundant points, and the vertical distance limit algorithm precisely removes the remaining redundant points. The study first determines the coordinates of each vertex in the sliding window, when the window slides to $[P_3, P_4, P_5, P_6, P_7]$, the equation of the line P_3P_7 is $cx - y + d = 0$, where the expressions of c and d are shown

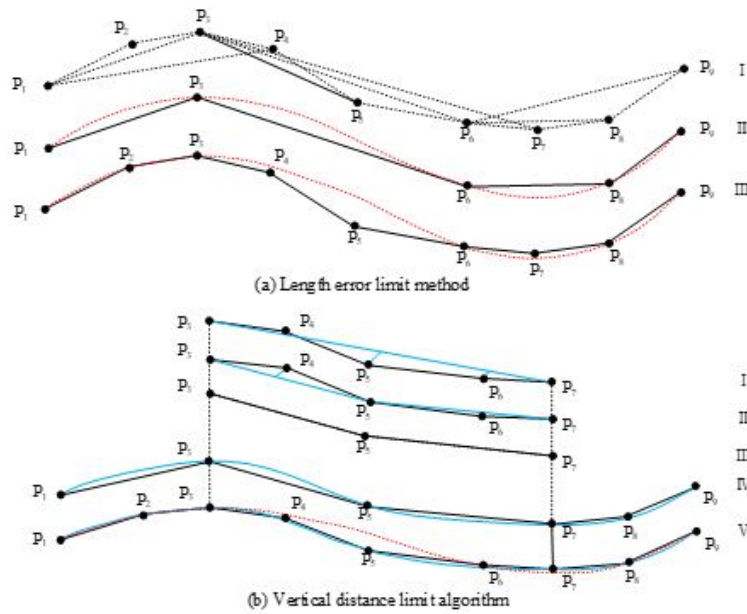


Fig. 3.1: Schematic diagram of length error limit algorithm and vertical distance limit algorithm based on sliding window

in equation (3.3).

$$\begin{cases} c = \frac{y_7 - y_3}{x_7 - x_3} \\ d = y_3 - \frac{y_7 - y_3}{x_7 - x_3} x \end{cases} \quad (3.3)$$

The study also needs to calculate the distances d_4, d_5 and d_6 from the points P_4, P_5 and P_6 in the window to the line $P_3 P_7$, see equation (3.4).

$$\begin{cases} d_4 = \frac{|cx_4 - y_4 + d|}{\sqrt{c^2 + (-1)^2}} \\ d_5 = \frac{|cx_5 - y_5 + d|}{\sqrt{c^2 + (-1)^2}} \\ d_6 = \frac{|cx_6 - y_6 + d|}{\sqrt{c^2 + (-1)^2}} \end{cases} \quad (3.4)$$

The study compared d_4, d_5 and d_6 with the vertical distance threshold d_ϵ , respectively, to obtain $d_4 < d_\epsilon, d_5 > d_\epsilon, d_6 < d_\epsilon$. Therefore, P_5 was chosen as the splitting point to split the sliding window into two parts, and a key vertex was added to the initial refinement to obtain significantly improved refinement results. The vertical threshold d_ϵ is determined in equation (3.5).

$$d_\epsilon = \gamma \cdot \eta \cdot (L/L_{sum} + \omega) \cdot \frac{300}{v + 150} \quad (3.5)$$

In Eq. (3.5), γ and η denote the streamlining control factor and error sign change factor, respectively. γ takes the values of $[0.5, 1.5]$ and β takes the values of 0.5 or 1. ω is the factor to correct L/L_{sum} . The study uses the streamlining ratio CR , the local maximum distance error E_{max} , and the overall length error E_l to evaluate the streamlining effect of the SWR algorithm, see equation (3.6).

$$\begin{cases} CR = N/C \\ E_{max} = \max_{1 \leq i \leq n} e_i \\ E_l = (L_n/L_c) * 100\% \end{cases} \quad (3.6)$$

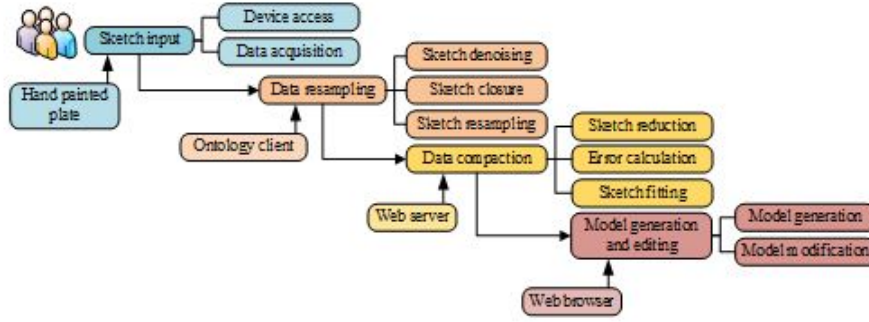


Fig. 3.2: HS 3D Lightweight Modeling Process

In Eq. (3.6), N and C denote the number of vertices before and after streamlining, respectively; e_i denotes the vertical Euclidean distance from a vertex of the original data to the streamlined curve; L_n denote the total length of the original HS trajectory and the total length of the streamlined data, respectively. After the streamlining of HS data, the study needs to stretch the processed data to generate 3D models. $z = 0$ Stretching sketch 3D modeling is mainly divided into Single-stroke Closed Sketch (SCS) and Single-stroke Unclosed Sketch (SUS) 3D modeling. The 2D contour points are $S_m = \{P_i : (x_i, y_i, z_i), i = 1, 2, 3, \dots, m, z_i = 0\}$, which are stretched in the positive direction of Z-axis, see equation (3.7).

$$\begin{cases} x = x \\ y = y \\ z = z + h \times d, i \in N \end{cases} \quad (3.7)$$

In Eq. (3.7), d and h are the stretch length and the number of copy translation layers, respectively, and the expression of the stretched 3D point cloud model is shown in Eq. (3.8).

$$S_{gm} = \begin{Bmatrix} P_{01}(x_1, y_1, 0) & P_{02}(x_2, y_2, 0) & \dots & P_{0m}(x_m, y_m, 0) \\ P_{11}(x_1, y_1, 0) & P_{12}(x_2, y_2, h) & \dots & P_{1m}(x_1, y_1, h) \\ \dots & \dots & \dots & \dots \\ P_{g1}(x_1, y_1, g * d) & P_{g2}(x_2, y_2, g * d) & \dots & P_{gm}(x_m, y_m, g * d) \end{Bmatrix} \quad (3.8)$$

$g = D/d$ in Eq. (3.8) is rounded. Since the beginning and end of SUS are not connected, it is not possible to obtain a closed 3D point cloud directly. The study transforms SUS into a closed figure by the offset point coordinate calculation method, and then follows the SCS stretching to generate a 3D point cloud method, so as to obtain the 3D modeling of SUS. The HS modeling process is mainly divided into four stages: sketch input, data pre-processing, data refinement, and model generation and editing, see Figure 3.2.

The modeling process in Figure 3.2 is as follows: first, the sketch data are collected by connecting the digital board, and the collected data are pre-processed by noise reduction, closure and real-time resampling using the ontology client, then the sampled data are streamlined by using the SWR algorithm, and finally they are input to the client browser to generate a lightweight 3D model.

3.2. Integration and Improvement of HS and LALS-LS ITL Model Construction. In addition to using HS for 3D modeling, the study uses LS equipment to obtain scan line point cloud data for 3D modeling[20]. There are more redundant points in the scan line point cloud data, so the data need to be streamlined by the Latitude And Longitude Simplification (LALS) method before actual use. The LALS method provides an efficient and accurate solution for point cloud data processing by combining meridian simplification based on chord height and latitude refinement based on adaptive layering. This method can effectively alleviate the problem of local hollowing in point clouds caused by chord height and angle deviation methods, while significantly reducing noise in point cloud data. Through adaptive layered slicing, the LALS method optimizes

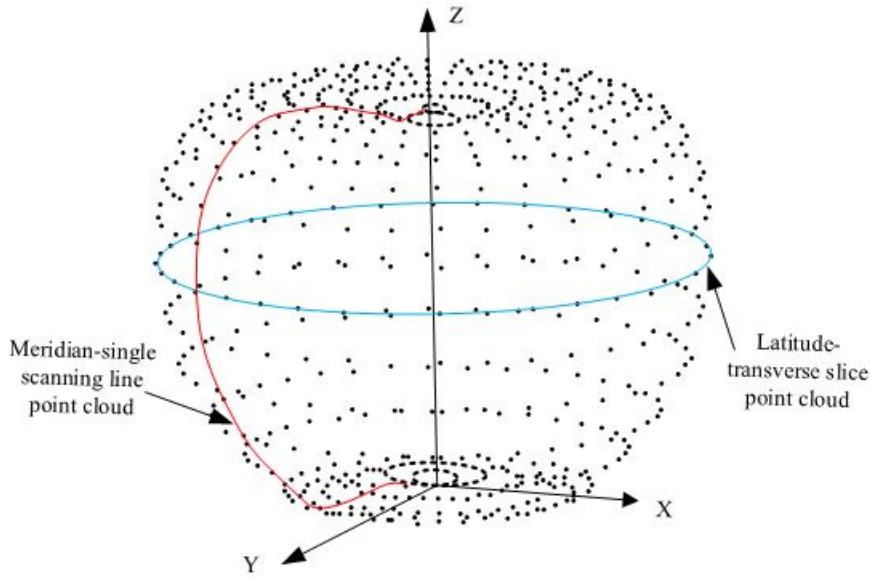


Fig. 3.3: Schematic diagram of point cloud LALS method

data reduction in the latitude direction, ensuring the integrity and accuracy of point cloud data and thereby improving the quality and efficiency of 3D modeling. In addition, the efficiency and accuracy demonstrated by this method in processing large-scale point cloud data greatly improve the reliability of subsequent 3D modeling and analysis. The point cloud LALS method is shown in Figure 3.3.

The LALS method in Figure 3.3 is mainly divided into the angle-chord height-based point cloud meridian refinement and the adaptive stratification-based latitude refinement method. The angle-chord height-based point cloud meridian streamlining method can improve the problem of local hollowness in the point cloud due to the deletion of too many points by the chord height method and the angle deviation method without significantly increasing the number of retained points and effectively remove the noise in the point cloud meridian direction. The adaptive layering-based weft line refinement method first requires adaptive layered slicing in the direction perpendicular to the scan line. Let the longitude line be parallel to z axis, and the latitude line be parallel to xy plane, then the point cloud layering direction is z axis direction, and the layering position is determined in equation (3.9).

$$Z_i = \begin{cases} Z_{\max}, & i = 0 \\ \sum_{j=1}^i o + Z_{\min}, & Z_i \leq Z_{\max} \\ Z_{\max}, & Z_i > Z_{\max} \end{cases} \quad (3.9)$$

In Eq. (9), o and Z_i are the layered thickness of the point cloud and the end position of the point cloud in the i layer, respectively. Z_{\max} and Z_{\min} denote the maximum and minimum values of the Z coordinates. After the adaptive layering process, the point cloud has a certain thickness and width. In order to reduce the computational effort, the projection method is used to extract the outer contour of the sliced point cloud data instead of the curve fitting method to improve the overall efficiency of the algorithm, and the projected planar sliced point cloud is stored in a data structure similar to the image raster grid column. For a sliced point cloud withn points $p(x_i, y_i)$, the point cloud is minimally enclosed by a rectangle of $L \times H$ and the rectangle is divided into an array of cells of $a \times b$, where the cell located in the i row and j column is noted as K_{ij} , and the expression of K_{ij} is given in equation (3.10).

$$K_{ij} = (i - 1) \cdot L + j \quad (1 \leq i \leq a, 1 \leq j \leq b) \quad (3.10)$$

The formula for the cell number F_i and column number P_i where any point $p(x_i, y_i)$ is located is shown in equation (3.11).

$$\begin{cases} F_i = \text{int}[(x_i - x_{\min}) / (L/b)] \\ P_i = \text{int}[(y_i - y_{\min}) / (H/a)] \end{cases} \quad (3.11)$$

In the formula (3.11), $\text{int}[]$ indicates the rounding function, L/b and H/a indicate the length and width of the cell respectively, and the serial number of the cell $K(p_i)$ see formula (3.12).

$$K(p_i) = (F_i - 1) \cdot L + P_i \quad (3.12)$$

After the gridding of the sliced point cloud data, the study also needs to use image processing techniques for binarization. In the process of gridding and binarization of the sliced point cloud data, the size of the grid size $S_{\text{cell}} = L/a = H/b$ directly determines the final degree of streamlining, and the formula for calculating S_{cell} is given in equation (3.13).

$$S_{\text{cell}} = \xi \sqrt{\frac{(x_{\max} - x_{\min})(y_{\max} - y_{\min})}{n}} \quad (3.13)$$

In Eq. (3.13), n and ξ denote the number of sliced points cloud data points and the scale adjustment factor, respectively, where ξ is mainly used to adjust the grid edge size. To comprehensively evaluate the streamlining effect of the LALS algorithm, the reduction ratio R_V , the streamlining error E_{dis} and the streamlining goodness index FOM_a are introduced in Eq. (3.14). R_V is defined as the volume ratio between the original and simplified datasets, mainly quantifying the degree of volume reduction during the data simplification process. E_{dis} measures the difference between the simplified dataset and the original dataset, reflecting the impact of the simplification process on data integrity. FOM_a is a comprehensive performance indicator that evaluates the effectiveness of algorithm simplification by considering both reduction rate and simplification error, to balance the efficiency of data simplification and the accuracy of results.

$$\begin{cases} R_V = \frac{V_1 - V_2}{V_1} * 100\% \\ E_{dis} = \frac{1}{V_2} \sum_{p \in S_2} d(p, S_1) \\ FOM_a = \frac{R_V}{E_{dis} \cdot T_S} \end{cases} \quad (3.14)$$

In Eq. (3.14), V_1 and V_2 denote the number of streamlined point clouds before and after streamlining, respectively, $d(p, S_1)$ denotes the Euclidean distance from a point in the point cloud S_2 to the nearest point in S_1 , and T_S is the point cloud streamlining processing time. Based on the final streamlined data, it is optimized by preliminary triangulation and minimum internal angle maximum criterion, and the final LS lightweight model is obtained. The LS lightweight modeling flow is shown in Figure 3.4.

The modeling process in Figure 3.4 consists of four steps: point cloud acquisition, point cloud preprocessing, point cloud refinement, and network reconstruction, firstly, the point cloud data is obtained by accessing the measurement equipment to scan the object, and then the point cloud data is preprocessed by the ontology client, and then the final refined point cloud data is obtained by adaptive layering and projection, and then the final LS lightweight model is obtained by fast triangulation and mesh optimization of these refined data. The evaluation of the lightweight effect of the ITL model can be expressed by the model size reduction ratio R_F , the lightweight error E_{Vol} , and the goodness of lightweight index FOM_b , as shown in equation (3.15). R_F is used to measure the ratio between the size of the lightweight model and the original model, which can reflect the reduced storage requirements during the lightweight process. E_{Vol} refers to the degree of difference in output results between the lightweight and original models used to evaluate the impact of lightweight on model performance. FOM_b is a comprehensive evaluation indicator that quantifies the overall effect of the lightweight process by balancing the model size reduction rate and lightweight error, to find the best balance between lightweight and performance loss.

$$\begin{cases} R_F = \frac{F_1 - F_2}{F_1} * 100\% \\ E_{Vol} = \frac{|Vol_1 - Vol|}{Vol_1} * 100\% \\ FOM_b = \frac{R_F}{E_{Vol} \cdot T_R} * 100\% \end{cases} \quad (3.15)$$

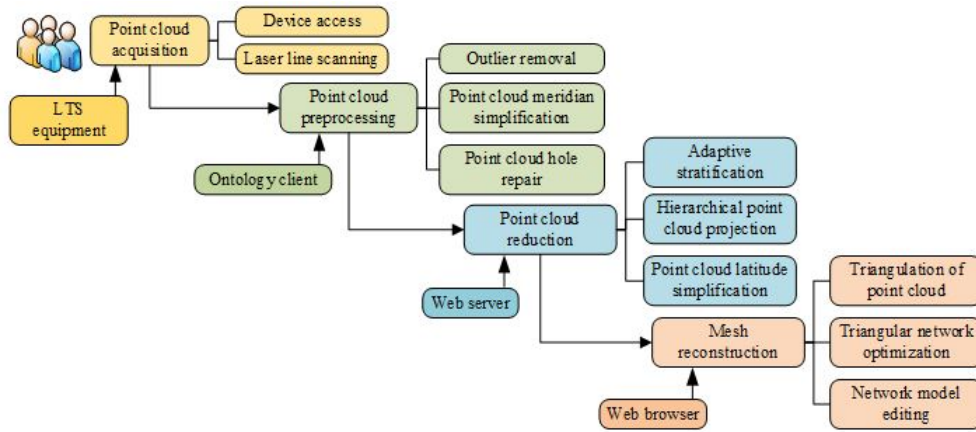


Fig. 3.4: LS lightweight modeling process

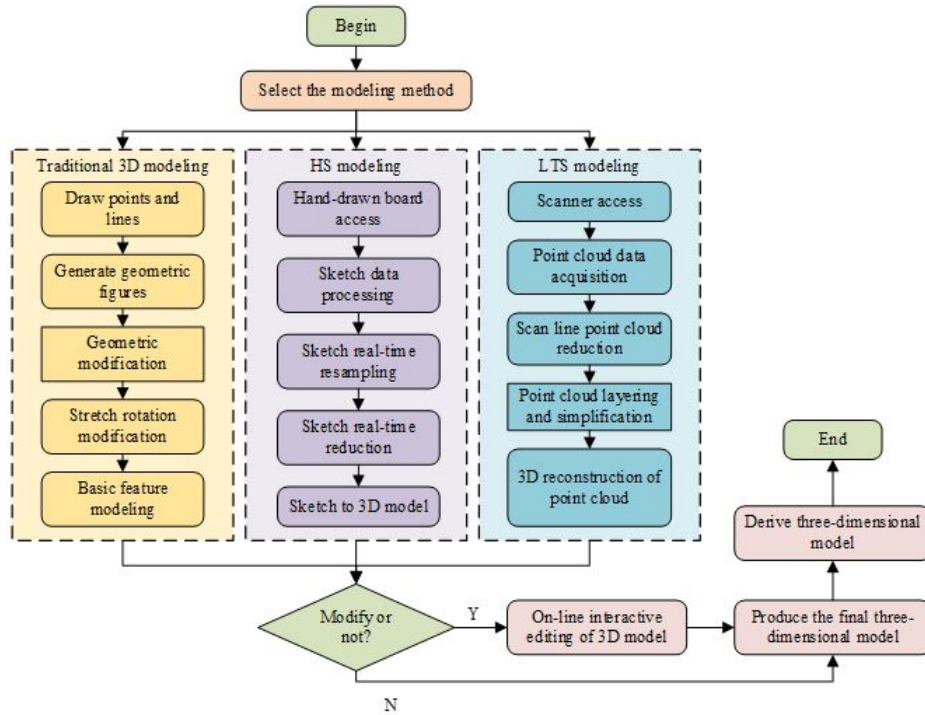


Fig. 3.5: 3D modeling process under different interaction modes

In Eq. (3.15), F_1 and F_2 denote the generated model file size before and after streamlining, respectively, Vol_1 and Vol_2 denote the generated model volume before and after point cloud streamlining, respectively, and T_R is the generated model time. For the needs of 3D modeling, the study constructs a combined HS and LS ITL modeling system based on traditional geometric modeling, see Figure 3.5 [1].

Figure 3.5 modeling process is as follows, first of all, Different modeling methods are selected according to the modeling objects, the regular geometric shape selected traditional 3D modeling, irregular shape selected HS

Table 4.1: Experimental parameter setting

Model	Parameter selection							
	I_ε	n	E_I	ε_1	ε_2	d_ε	γ	ω
HS	χ	n	ε_1	ε_2	γ	η	ω	
	1.0	0.5	1%	5%	1.0	0.5	0.5	
LS	h	D	D	α	δ	η		
	0.1mm	123.8 mm	0.74mm	15°	0.45mm	0.4		

modeling, need to reverse the existing physical creation of data models selected LS modeling. After the study determines the modeling method and the initial model, it is necessary to use the 3D model online interactive editing to improve the model construction further, to get the final ITL modeling system. ITL modeling system can record the real three-dimensional information of the scene and input it into the system to create a data model in reverse, then scale, rotate, and translate the scene in the system to highlight the contrast between reality and reality of artworks.

4. Results. To validate the performance of the ITL modeling system, the study conducts experiments on HS and LS models separately. This section focuses on preparing the experimental data and analyzing the performance of both models based on the streamlining algorithm.

4.1. ITL modeling system experimental data preparation. In the experimental data preparation stage, to comprehensively evaluate the adaptability of the model processing algorithm to different geometric features, the selected experimental graphics of the HS model include the number 8-shaped, multi-arc, chromosome, and serrated leaves. The experimental object of the LS model is the Stitch model $70.2mm \times 84.7mm \times 123.8mm$, which was selected because its complexity is moderate and can effectively test and demonstrate the performance of the algorithm when dealing with practical models with a certain level of complexity. The parameters of the HS and LS models were set, as shown in Table 4.1.

In Table 4.1, h is the highest accuracy of the 3D scanner, D is the height of the Stitch model as the scanned object, d , α and δ denote the chord height threshold, angle threshold and maximum radial width threshold, respectively, and the number of vertices of the point cloud model is 42852 when $\xi=0.4$ is used. Sampling (RS) method, Uniform Grid (UG) method, Discrete Curvature (DC) method and Local Density (LD) method are used to compare with the LALS algorithm. The evaluation metrics based on HS model are resampling ratio SR , CR , E_{max} , E_l , η_F , and η_S . The evaluation metrics based on the LS model are data simplification metrics R_V and R_F , accuracy metrics E_{dis} and E_{Vol} , runtime metrics T_S and T_R , and goodness indices FOM_a and FOM_b . The experimental parameter settings in Table 1 aim to provide consistent evaluation criteria for the HS model and LS model. The setting of HS model parameters reflects the adaptability and flexibility of the algorithm when processing point cloud data with different shapes. In order to ensure that sufficient model details are captured, and considering computational efficiency and practicality of model processing, the LS model parameters were selected with the values shown in Table 1.1. By setting these parameters and selecting diverse experimental subjects, the study aims to comprehensively evaluate the performance of various algorithms in data simplification, accuracy preservation, and computational efficiency.

4.2. Performance analysis of HS model based on resampling and SWR algorithm. To verify the performance of the real-time resampling algorithm of the HS model, the study plots the contour curves of four graphs at the speed of $150px/s$, $2004px/s$, $300px/s$, $400px/s$, and $500px/s$ respectively.

Figure 4.1 shows the real-time resampling results for the four shapes. SR decreases as the hand-drawing speed increases over a range. When the hand-drawing speed is $150px/s$, the value of SR is 3.09 for chromosome, 3.05 for figure-8, 3.04 for *saw* tooth leaf, and 2.93 for multi-circle arc. When the hand-drawing speed is $500px/s$, the value of SR is 1.01 for chromosome, 1.02 for figure-8, 1.01 for sawtooth leaf, and 1.00 for multi-circle arc. It is proved that the real-time resampling algorithm can effectively reduce the amount of redundancy in the original data.

To verify the effectiveness of the SWR algorithm, the data refinement results of the four figures at different

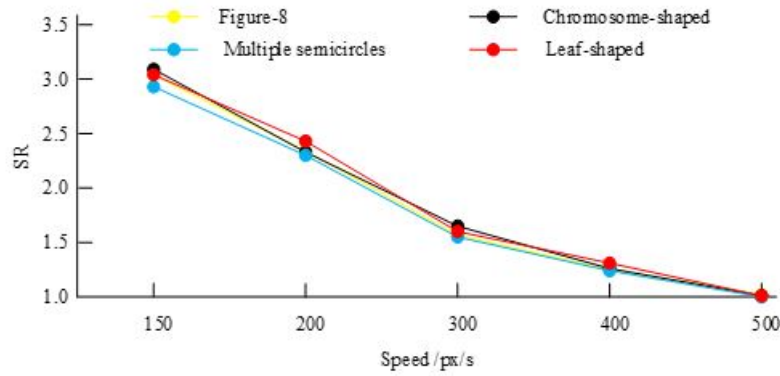


Fig. 4.1: Real-time resampling results of four graphs

Table 4.2: Generation time of HS 3D model

Time/ms		Figure 8	Chromosome-shape	Multiple semicircles	Leaf-shaped
Before streamlining	Total time	1285	2101	2361	3524
	Mean time	264	425	474	716
Streamlined	Total time	481	801	932	1253
	Mean time	97	164	174	251
Reduce percentage		65.53%	61.41%	63.29%	64.94%

hand-drawing speeds are shown in Fig. 4.2. Fig. 4.2(a) shows the variation curves of for the four figures. The mean values of CRCR for the figure- 4.3, chromosome, multicircular arc, and serrated leaf shapes are 3.67, 3.85, 3.61, and 3.82. Fig. 4.2(b) shows the variation curves of E_{max} for the four sketches. The mean values of for the figure- 4.3, chromosome, multicircular arc, and serrated The mean values of E_{max} are 0.75, 1.33, 1.43, and 1.05 for figure- 4.3, chromosome, multi-circular arc, and serrated leaf shapes, respectively. Figure 4.2(c) shows the variation curves of E_l for the four sketches, and the values of E_l are 0.98%, 2.80%, 3.71%, and 3.02% for figure- 4.3, chromosome, multi-circular arc, and serrated leaf shapes, respectively. It can be seen from the figure that the overall error and local error of the figure 8 shape are smaller than the other three sketches.

Figure 4.3 shows the 3D model lightening results of different shapes before and after data refinement at a hand-drawing speed of $300px/s$, where F_1 , F_2 , S_1 , and S_2 indicate the number of triangular surface pieces and model size before and after data refinement, respectively. Figure 4.3(a) shows the results of F_1 , F_2 , η_F for the four graphical generation models. The values of F_1 are 1541, 2580, 3016 and 3874 for figure- 4.3, chromosome, multi-circular arc and sawtooth leaf shapes, respectively; the values of F_2 are 490, 768, 965 and 1428, respectively; and the values of η_F are 68.20%, 70.23%, 68.00% and 63.14%, respectively. Figure 4.3(b) shows the S_1 , S_2 and η_S results for the four graphical generation models. The values of S_1 , S_2 and η_S are 77.7KB, 26.3KB and 66.11% for the figure- 4.3 shape respectively, the values of S_1 , S_2 and η_S are 128.4KB, 41.2KB and 67.91% for the chromosome shape respectively, the values of S_1 , S_2 and η_S are 150.4KB, 52.3KB and 65.23% for the multicircular arc shape respectively, and the values of S_1 , and for the serrated leaf shape respectively, S_2 and η_S are 191.6KB, 71.5KB, and 62.68%, respectively. To verify the fluency of the HS model based on the SWR algorithm, the model generation time before and after the streamlining of 10 sets of HS data was selected for the study, and the average value was taken as the final result, which is shown in Table 4.2.

Table 4.2 shows the experimental results of the time required for the four graph generation models. The average time before and after streamlining for the figure-8 shape is 264 ms and 97 ms, respectively; the average time before and after streamlining for the chromosome shape is 425 ms and 164 ms, respectively; and the average time before and after streamlining for the multi-circle arc shape is 474 ms and 174 ms, respectively. The average time reduction percentages for each graph are 65.53%, 61.41%, 63.29%, and 64.94%, respectively.

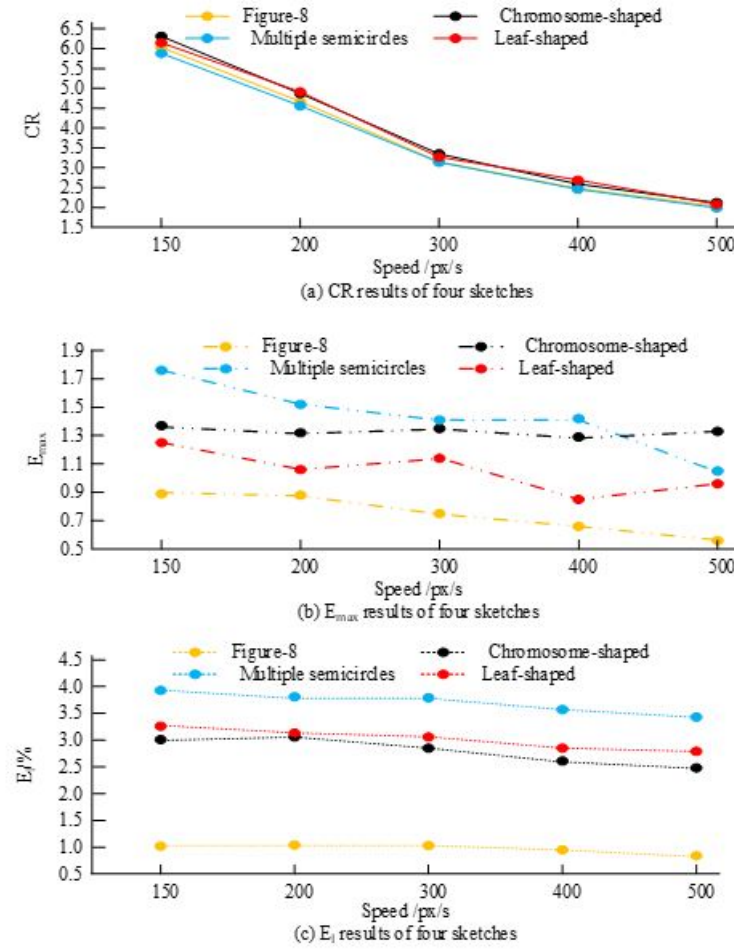


Fig. 4.2: Real-time reduction results of four graphics

Combining these results, it can be concluded that the SWR algorithm proposed in the study can effectively improve the model data processing speed.

Figure 4.4 shows the comparison of the effects of the 3D models generated before and after data reduction for the sketches of "Number 8", "Colored Body", "Multi Circular Arc", and "Sawtooth Leaf". Through simplification, the model significantly reduces the amount of data while retaining key geometric features and overall shape. This not only improves the processing and rendering speed of the model but also optimizes storage efficiency while ensuring high-quality visual representation. In addition, the simplified model still has rich details and accurate morphology.

4.3. Analysis of LS model application based on LALS algorithm. In order to comprehensively compare the performance advantages and disadvantages of LALS algorithm with other algorithms, the study was conducted by scanning the physical objects to obtain 152, 944 point clouds of raw data, and experiments were conducted using RS, UG, DC and LD, and the experimental results are shown in Figure 4.4 and Figure 4.5.

Figure 4.5 shows the performance comparison results of five algorithms in point cloud refinement processing, including the comparison of reduction rate R_{V4} and simplification error E_{dis} (Figure 4.5 (a)), as well as the comparison of processing time T_S and simplification goodness index FOM_a (Figure 10 (b)). In terms of R_V , LALS, RS, UG, DC, and LD algorithms exhibit similar performance, reaching 71.99%, 71.95%, 71.88%,

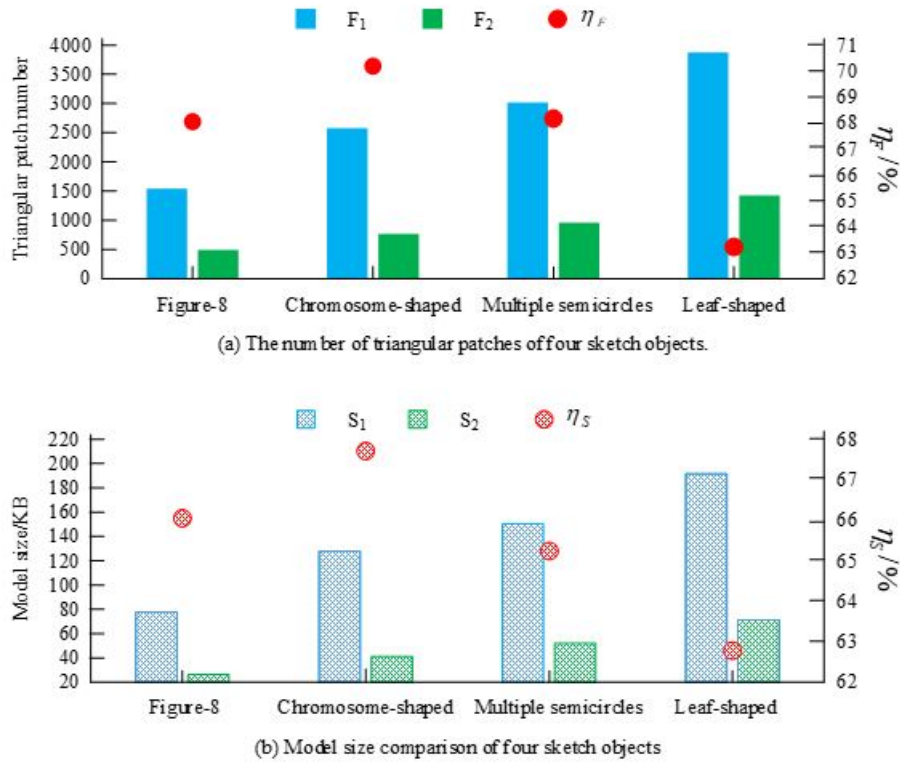


Fig. 4.3: Lightweight results of the model before and after data reduction

71.94%, and 71.97% respectively, indicating that these algorithms have similar efficiency in reducing data volume. However, on E_{dis} , the performance of the LALS algorithm is superior to other algorithms, with a value of 0.1724mm, which is lower than the error values of RS and UG (0.2688mm and 0.2609mm, respectively), but slightly higher than the DC and LD algorithms of 0.1167mm and 0.1104mm, indicating that the LALS algorithm has better performance in maintaining the accuracy of point cloud data. T_S and FOM_a further evaluated the comprehensive performance of the algorithm. The processing time of the LALS algorithm is 1.363 seconds, slightly higher than that of the RS and UG algorithms, but the highest FOM_a value is obtained, reaching 3.06, reflecting its good balance between efficiency and refinement effect. In contrast, although the processing time of DC and LD algorithms exceeds 2 seconds, their FOM_a values are 2.74 and 2.88, respectively, indicating that they have lower efficiency while maintaining high refinement effects. As a result, the LALS algorithm has shown relatively balanced performance in point cloud refinement tasks, especially in maintaining low simplification errors and achieving high simplification goodness indicators.

Figure 4.6 shows the performance of five different algorithms in model lightweight tasks. Figure 4.6 (a) evaluates the model from two dimensions: reduction factor R_F and additional volume ratio E_{Vol} . In terms of R_F , the performance of algorithms is similar, with the RS algorithm accounting for 70.14%, slightly better in reducing model volume. The lowest R_F of the LD algorithm is 69.65%. In terms of E_{Vol} , the DC and LD algorithms perform well, with values of 0.0252% and 0.0236%, respectively, indicating that these two algorithms minimize additional changes to the model shape while reducing the model volume, maintaining high fidelity of the original model. Figure 4.6 (b) further compares the results of processing time T_R and lightweight optimization index FOM_b , revealing the relationship between algorithm efficiency and lightweight quality. In terms of T_R , the LALS algorithm significantly outperforms other algorithms with a processing time of 3.405 seconds, while the processing time of RS, UG, DC, and LD algorithms exceeds 4 seconds, indicating that the LALS algorithm has higher computational efficiency while maintaining lightweight performance. From the

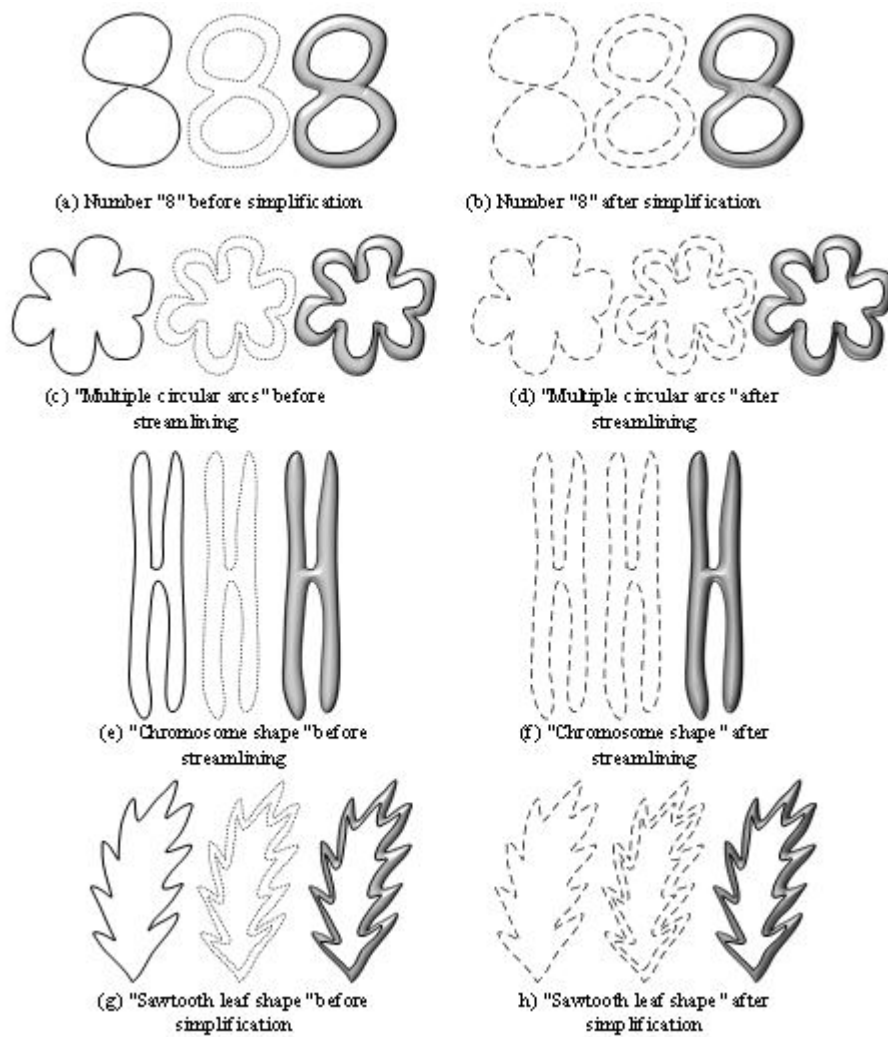


Fig. 4.4: Three-dimensional models generated from four types of images

FOM_b value, it can be seen that the LALS algorithm outperforms other algorithms with a score of 712.51, reflecting its optimal performance in overall efficiency and lightweight quality during the model lightweight process. As a result, the LALS algorithm has shown superior comprehensive performance in model lightweight, not only comparable to other algorithms in aspect R_F but also the outstanding performance in E_{Vol} and T_R metrics, while maintaining a relatively low FOM_b . The above results highlight the efficiency and superiority of the LALS algorithm in the lightweight process of LS models generated from simplified point cloud data.

5. Discussion and Conclusion. In the field of art design, the application of virtual and real scenes is essential. With the emergence of 3D printing technology, creators use 3D modeling software to complete the processing of virtual and real scenes of their works, thus making the works more three-dimensional and beautiful. Traditional 3D modeling software has weak human-computer interaction and cumbersome functions, and the collected raw data also has more noise and redundant points, which is not conducive to the rendering of the model. To address this problem, the study proposes a modeling system that combines the HS model based on the SWR algorithm and the LS model based on the LALS algorithm to obtain ITL modeling system on the

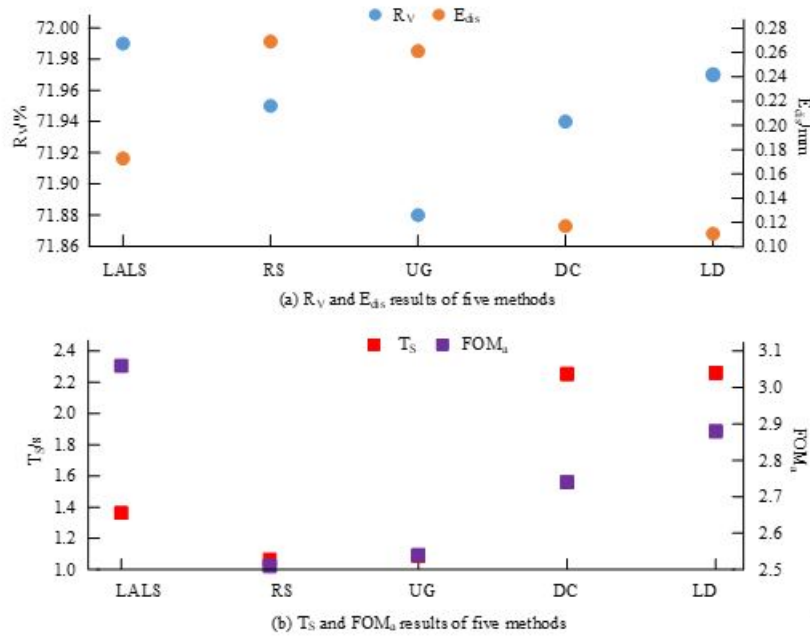


Fig. 4.5: Point Cloud Simplification Results of Five Algorithms

basis of traditional 3D modeling. The results show that the average values of E_l and E_{max} for figure 4.3 shapes by SWR algorithm are 0.98% and 0.75, respectively, which are lower than 3.71% and 1.43 for multi-circular arc shapes. When the hand-drawing speed is 300px/s, the values of η_F and 65.48% for the HS model based on SWR algorithm are 67.39% and η_S , and the time required to generate the model is reduced by 63.79% compared with that before the refinement. In the point cloud data refinement of the LS model, the values of R_V and FOM_a of the LALS algorithm are 71.99% and 3.06, respectively, which are 0.11% and 0.52 better than the UG algorithm. The value of R_F of LS model based on LALS algorithm is 69.92%, which is higher than 69.81% of UG algorithm, and the value of FOM_b is 712.51, which is higher than 329.17 of UG algorithm.

The proposed modeling system demonstrates significant advantages in virtual and real scene processing in the field of art and design by combining the HS model based on the SWR algorithm with the LS model based on the LALS algorithm. The introduction of the SWR algorithm and LALS algorithm not only optimizes the human-computer interaction interface of traditional 3D modeling software but also effectively reduces noise and redundant points in model data, thereby improving the efficiency and quality of model rendering. The application of SWR and LALS algorithms in the field of art and design has significantly improved the efficiency and quality of the transformation of artworks from virtual to physical. This method optimizes the human-computer interaction interface, allowing artists to create more intuitively and flexibly while ensuring the details and realism of the work. Through this technological advancement, the creative process of art and design works has become more efficient, and the expressive power of the works has been significantly enhanced, providing artists with broader creative space and possibilities.

In addition, there is still room for expansion in the potential applications and algorithm improvements of the proposed method in industrial prototype design, medical modeling, and other fields. In the field of industrial design and prototype manufacturing, high precision and model quality are required. The application of SWR and LALS algorithms can provide high-quality model data for rapid prototyping of complex parts. By further optimizing the algorithm to adapt to the printing characteristics of specific materials, printing efficiency, and prototype accuracy can be significantly improved. In addition, in the field of medical modeling, especially in personalized medical device design and biological tissue printing, the application of these algorithms is expected

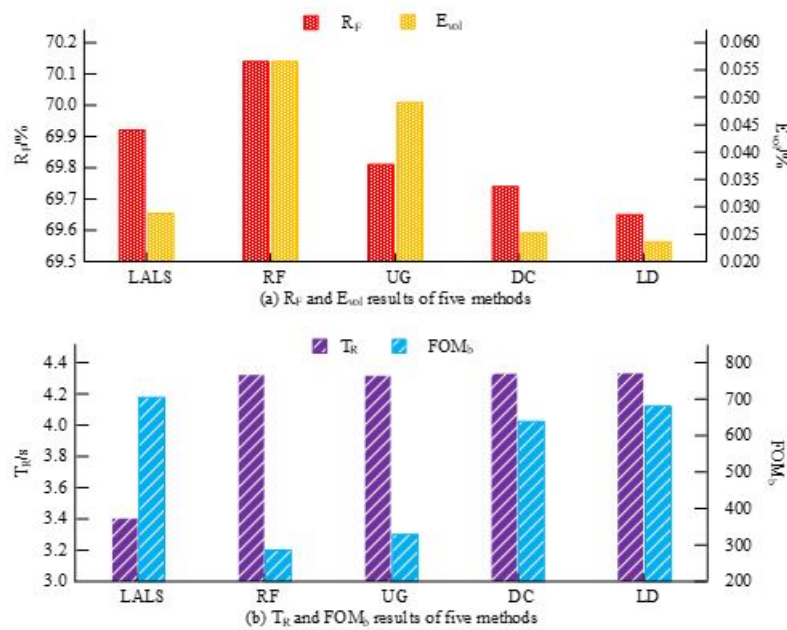


Fig. 4.6: Lightweight results of the model based on five algorithms

to improve the precision of tissue structure models and promote the development of medical model printing technology.

Although research has achieved certain results, there are certain limitations in experimental settings and algorithm design. The efficiency and accuracy of algorithms in handling extremely complex models still need to be improved. In response to this limitation, future research can consider introducing advanced technologies such as machine learning to automatically optimize parameter selection during model processing, further improving the adaptability and efficiency of the algorithm. Future research directions also include in-depth optimization and improvement of algorithms, such as introducing more advanced data compression techniques further to reduce the noise and redundancy of model data, or developing new algorithms to support real-time rendering of dynamic models better.

REFERENCES

- [1] J. C. R. ALCANTUD, *Convex soft geometries*, Journal of Computational and Cognitive Engineering, 1 (2022), pp. 2–12.
- [2] J. BAI, W. ZHOU, J. TUO, AND F. QIN, *End-to-end sketch-3d model retrieval with spatiotemporal information joint embedding*, Journal of Computer-Aided Design & Computer Graphics, 33 (2021), pp. 826–836.
- [3] H. CHEN, Z. WEI, X. LI, Y. XU, M. WEI, AND J. WANG, *Repcd-net: Feature-aware recurrent point cloud denoising network*, International Journal of Computer Vision, 130 (2022), pp. 615–629.
- [4] CLAYTON EWAN EWAN, *The virtual and the real. digital culture and the body in the study of handwriting*, Open Information Science, 5 (2021), pp. 11–26.
- [5] H. FANCOURT, J. LYNCH, J. BYRD, AND C. STEPHAN, *Next-generation osteometric sorting: using 3d shape, elliptical fourier analysis, and hausdorff distance to optimize osteological pair-matching*, Journal of Forensic Sciences, 66 (2021), pp. 821–836.
- [6] T. ITO, T. KANEKO, Y. TANAKA, AND S. SAGA, *An interactive sketch-based cad interface realizing geometrical and topological editing across multiple objects based on fuzzy logic*, Computers & Graphics, 103 (2022), pp. 153–167.
- [7] W. KOC, *Analysis of the effectiveness of determining the horizontal curvature of a track axis using a moving chord*, Problemsmy Kolejnictwa - Railway Reports, 65 (2021), pp. 77–86.
- [8] A. S. NATERI, E. HASANLOU, AND A. HAJIPOUR, *Prediction of nanosilver and dye content on silk fabric using a scanner-based artificial intelligence technique*, Pigment and Resin Technology, 51 (2021), pp. 372–380.
- [9] C. PAN, J. HUANG, J. GONG, AND C. CHEN, *Teach machine to learn: hand-drawn multi-symbol sketch recognition in one-shot*,

- Applied Intelligence, 50 (2020), pp. 2239–2251.
- [10] F. PISTILLI, G. FRACASTORO, D. VALSESIA, AND E. MAGLI, *Learning robust graph-convolutional representations for point cloud denoising*, IEEE Journal of Selected Topics in Signal Processing, 15 (2021), pp. 402–414.
 - [11] R. SARVADEVABHATLA, S. SURYA, T. MITTAL, AND R. BABU, *Pictionary-style word guessing on hand-drawn object sketches: Dataset, analysis and deep network models*, IEEE Transactions on Pattern Analysis and Machine Intelligence, 42 (2020), pp. 221–231.
 - [12] X. SHI, H. CHEN, AND X. ZHAO, *Rebor: A new sketch-based 3d object retrieval framework using retina inspired features*, Multimedia Tools and Applications, 80 (2021), pp. 23297–23311.
 - [13] F. M. VIVALDI, A. DALLINGER, A. BONINI, N. POMA, L. SEMBRANTI, D. BIAGINI, P. SALVO, F. GRECO, AND F. FRANCESCO, *Three-dimensional (3d) laser-induced graphene: structure, properties, and application to chemical sensing*, ACS Applied Materials & Interfaces, 13 (2021), pp. 30245–30260.
 - [14] Q. WU, J. LIU, Y. JIN, Y. CHEN, L. DU, AND L. M. WAQAS, *Thickness measurement method for the thermal protection layer of a solid rocket motor based on a laser point cloud*, Insight: Non-Destructive Testing and Condition Monitoring, 64 (2022), pp. 219–228.
 - [15] P. XU, T. HOSPEDALES, Q. YIN, Y. SONG, T. XIANG, AND L. WANG, *Deep learning for free-hand sketch: A survey*, IEEE Transactions on Pattern Analysis and Machine Intelligence, 45 (2022), pp. 285–312.
 - [16] P. XU, C. K. JOSHI, AND X. BRESSON, *Multigraph transformer for free-hand sketch recognition*, IEEE Transactions on Neural Networks and Learning Systems, 33 (2021), pp. 5150–5161.
 - [17] L. YANG, F. MAYER, U. BUNZ, E. BLASCO, AND M. WEGENER, *Multi-material multi-photon 3d laser micro- and nanoprinting*, Light: Advanced Manufacturing, 2 (2021), pp. 296–312.
 - [18] M. ZAGORSKI, G. TODOROV, N. NIKOLOV, Y. SOFRONOV, AND M. KANDEVA, *Investigation on wear of biopolymer parts produced by 3d printing in lubricated sliding conditions*, Industrial Lubrication and Tribology, 74 (2022), pp. 360–366.
 - [19] J. ZAN, *Research on robot path perception and optimization technology based on whale optimization algorithm*, Journal of Computational and Cognitive Engineering, 1 (2022), pp. 201–208.
 - [20] Z. H. ZHANG, *Point cloud data processing of three-dimensional reconstruction model of object by 3d laser scanning*, Nonlinear Optics, Quantum Optics, 52 (2020), pp. 205–217.

Edited by: Mudasir Mohd

Special issue on: Scalable Computing in Online and Blended Learning Environments: Challenges and Solutions

Received: Nov 10, 2023

Accepted: May 9, 2024